

The high-resolution diffraction beamline P08 at PETRA III

O. H. Seeck,^{a*} C. Deiter,^a K. Pflaum,^a F. Bertam,^a A. Beerlink,^a H. Franz,^a J. Horbach,^a H. Schulte-Schrepping,^a B. M. Murphy,^b M. Greve^b and O. Magnussen^b

^aHamburger Synchrotronstrahlungslabor am Deutsches Elektronen-Synchrotron DESY, Notkestrasse 85, 22607 Hamburg, Germany, and ^bIEAP, Christian-Albrechts-Universität zu Kiel, 24098 Kiel, Germany. E-mail: oliver.seeck@desy.de

The new third-generation synchrotron radiation source PETRA III located at the Deutsches Elektronen-Synchrotron DESY in Hamburg, Germany, has been operational since the second half of 2009. PETRA III is designed to deliver hard X-ray beams with very high brilliance. As one of the first beamlines of PETRA III the high-resolution diffraction beamline P08 is fully operational. P08 is specialized in X-ray scattering and diffraction experiments on solids and liquids where extreme high resolution in reciprocal space is required. The resolving power results in the high-quality PETRA III beam and unique optical elements such as a large-offset monochromator and beryllium lens changers. A high-precision six-circle diffractometer for solid samples and a specially designed liquid diffractometer are installed in the experimental hutch. Regular users have been accepted since summer 2010.

Keywords: beamline; X-ray diffraction; optics; monochromator; diffractometer.

1. Introduction

The use of highly brilliant synchrotron X-radiation is required for investigating bulk, surface and interface properties of liquid and solid samples. For this, the new third-generation synchrotron radiation source PETRA III (Balewski *et al.*, 2004) has been built at the research center DESY in Hamburg, Germany. PETRA III is especially designed to generate X-ray beams with very small divergence and source size, high intensity and very good coherence properties. The PETRA III experimental hall spans an octant of the storage ring with 2304 m circumference. Nine sectors for X-ray and VUV experiments have been set up. They are equipped with either one long undulator (5 m or longer) or two 2 m undulators as X-ray sources. In the latter case both 2 m undulators are oriented not exactly in-line but horizontally canted by 5 mrad. This canting angle is sufficiently large to install two completely independent beamlines of length more than 100 m in one sector. This is the case at sector 6 with the two beamlines P08 and P09 for X-ray scattering and diffraction applications. Beamline P08 is designed for experiments which require very high resolving power in reciprocal space and/or in real space whereas P09 utilizes resonant diffraction methods.

At P08 the X-ray beam parameters are tunable over a wide range with respect to photon energy, beam size, divergence and photon energy bandwidth. The beam size (FWHM) at the sample can be as small as $30\ \mu\text{m} \times 2\ \mu\text{m}$ and at maximum

$1.5\ \text{mm} \times 1\ \text{mm}$ (horizontal \times vertical). On collimation the divergence is as low as $10\ \mu\text{rad} \times 2\ \mu\text{rad}$ (FWHM). The typical flux of 10^{10} – 10^{12} photons s^{-1} strongly depends on the set-up. The photon energy can be tuned between 5.4 keV and 29.4 keV with an energy resolution $\Delta E/E \simeq 10^{-5}$ to 5×10^{-5} . Details and a complete summary are presented later in this article.

In the experimental area a high-precision six-circle diffractometer and a liquid diffractometer (Murphy *et al.*, 2012) are installed. Many different methods for investigating bulk, surfaces and interfaces of solids and liquids are available. Diffraction-based methods are single-crystal and powder diffraction, crystal truncation rod measurements, grazing-incidence diffraction and X-ray standing-wave measurements. Scattering-based methods are reflectivity and, preferably in combination with diffraction methods, standard small-angle scattering (SAXS) and grazing-incidence small-angle scattering (GISAXS).

2. Scope of beamline P08

High-resolution X-ray diffraction (HRXRD) is traditionally used for precise measurements of lattice parameters and is widely used as a standard tool for structural investigations. HRXRD allows the determination of physical parameters of single crystals, for instance thermal expansion coefficients and phase transition parameters. Also, precise measurements of

strain and stress distribution at the level of relative lattice parameter variations of 10^{-4} – 10^{-6} in the bulk and at interfaces are possible. Lattice distortions induced by various defects can be studied from their influence on the shape and the width of reflection profiles.

Investigations using HRXRD cover different length scales:

(i) Atomic scale. The atomic structure and charge density in bulk and layers as well as at surfaces and interfaces can be resolved by X-ray diffraction methods. It is the most accurate probe to determine the positions, occupation factors and displacement parameters of atoms within the unit cell. Even charge density studies on the level of binding electrons are feasible.

(ii) Nanometer scale. For structures at solid and liquid surfaces and at buried interfaces HRXRD allows one to define parameters such as thickness, orientation, chemical composition and interface roughness of layers. By variation of the incidence angle in reflectometry and grazing-incidence diffraction/scattering, depth-resolved studies can also be carried out. Two-dimensional reciprocal-space mapping methods can be used to investigate anisotropic sample surfaces.

(iii) Micrometer scale. Structural parameters of periodic and non-periodic nanostructures and organic/inorganic material systems at mesoscopic length scales can be investigated. For these techniques reciprocal- and real-space mapping is standard.

High resolution can be defined in real space (such as sub-nanometer resolution) or in reciprocal space having in mind that real space and reciprocal space are linked by a Fourier transformation. In contrast to many other beamlines, at P08 high resolution is available in real *and* in reciprocal space. This requires extraordinary accurate translations and rotations over a very large range in all degrees of freedom. For this reason, P08 is equipped with high-precision diffractometers which enable the users to position and orient the sample and the X-ray beam without any severe restrictions.

In addition to HRXRD, P08 has other scattering methods available which enable the users to investigate also amorphous or liquid samples in all varieties, such as standard SAXS and GISAXS. With some restrictions, basic spectrometric methods such as fluorescence analysis and anomalous scattering can be used as a supplement.

3. The storage ring PETRA III

The PETRA III storage ring is a third-generation synchrotron radiation source. It delivers X-ray beams from the VUV range (some hundred eV) to the hard energy range (some hundred keV) (Balewski *et al.*, 2004). In this photon energy range the beam parameters are optimized in terms of the following parameters: flux (defined as the number of photons per time) $N_{\text{ph}} t^{-1}$, beam size in the horizontal and vertical direction $\sigma_{h,v}$, divergence $\sigma'_{h,v}$, and energy band width b_w . The average brilliance or spectral brightness B is defined as

Table 1

Overview of the relevant PETRA III ring parameters (Brefeld, 2010).

The current is 100 mA during the first phase and will be 200 mA at a later stage. The β -functions are listed in Table 2.

Circumference	2304 m
Particle energy	6 GeV
Particle current	100 (200) mA
Horizontal emittance	1 nm rad
Coupling constant	0.01
Bunch length	13.2 mm
Number of bunches (continuous)	960
Number of bunches (timing)	40

Table 2

List of the β -functions at PETRA III at a sector with 2 m undulators and r.m.s. values of the photon beam size (in μm) and divergence (in μrad) at the source position [calculations for 12 keV (Brefeld, 2010)].

The indices h and v correspond to the horizontal and vertical, respectively. P08 is at a high- β sector.

	β_h (m)	β_v (m)	$\sigma_{s,h}$ (μm)	$\sigma_{s,v}$ (μm)	$\sigma'_{s,h}$ (μrad)	$\sigma'_{s,v}$ (μrad)
Low- β	1.2	4	35	6.5	29	5.3
High- β	20	2.4	142	5.2	8.7	5.5

$$B = \frac{N_{\text{ph}}}{t \sigma_h \sigma_v \sigma'_h \sigma'_v b_w} \quad (1)$$

with the usual units $1/[\text{s mm}^2 \text{ mrad}^2 (0.1\% \text{ bandwidth})]$ and is the most important figure of merit of an X-ray source (*e.g.* Thompson & Vaugan, 2001). The brilliance is determined by the storage-ring parameters and the insertion device which produces the X-radiation. In the case of PETRA III the insertion devices are undulators. The ring parameters which are relevant for the X-ray beam properties are listed in Table 1. The beam size and the divergence are functions of the emittance, the betatron-function (also called β -function; see, for example, Wiedemann, 2003) and undulator parameters.

Compared with other third-generation sources with particle energy between 6 and 8 GeV, PETRA III has the lowest horizontal emittance and coupling value. Using adequate undulators as X-ray sources, superior beam quality can be achieved. The smaller beam size and the smaller beam divergence make for a small emittance value. Therefore, at comparable integrated photon flux, the brilliance is raised to high values (see Fig. 1).

The brilliance is a generalized number with no information about the single-beam properties such as integrated flux, beam size or divergence. However, for typical scattering experiments these values are of great importance as they determine the ability to focus or collimate the beam. The photon source parameters are simple functions which are determined by the storage-ring settings: the β -function at the undulator cell and the emittance (Wiedemann, 2003). At PETRA III the β -function can be tuned by quadrupole magnets, independently at each of the undulator cells, and a so-called high- β and low- β tuning is provided. High- β in this context means well collimated but relatively large beams, whereas low- β means the opposite. Table 2 lists the source parameters of a 2 m-long

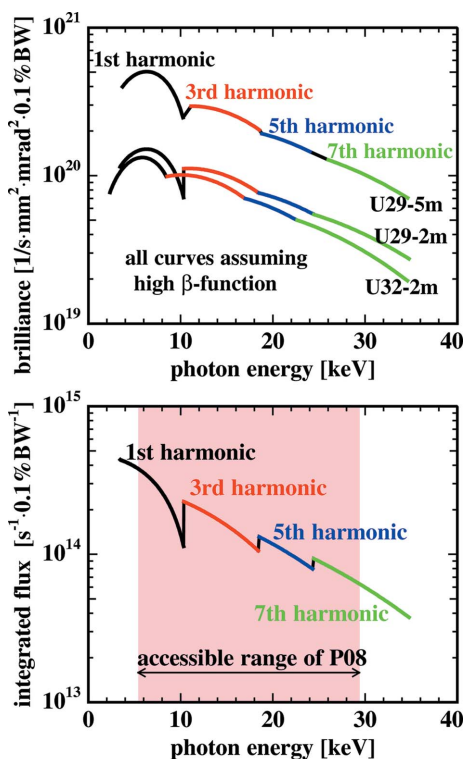


Figure 1
 Top: brilliance plots of selected undulators at PETRA III at 100 mA and high- β sectors. Bottom: integrated flux (central cone) of the beam as generated by the undulator U29-2 at beamline P08 (calculated). The first harmonic is called the ‘fundamental’ in the text [calculated using *SPECTRA* (Tanaka & Kitamura, 2001)].

PETRA III standard undulator U29 (Barthelmeß *et al.*, 2008) depending on the β -function.

4. Set-up of beamline P08

Sector 6 at PETRA III hosts the beamlines P08 and P09. Both are diffraction beamlines, P08 focusing on high-resolution diffraction and liquid scattering and P09 on resonant scattering. Both experimental set-ups are bulky. Therefore, the separation of 5 mrad given by the canting angle of the undulators is not sufficient. To increase the distance between the beams of P08 and P09 an optical device is introduced to P08 which creates a large vertical offset. These constraints determine the set-up of beamline P08 along with the requirements in obtaining high resolution in real and reciprocal space.

Beamline P08 has five major sections:

- (i) X-ray source (undulator) and the front-end, containing the white-beam slits and safety equipment.
- (ii) Optics hutch, containing the monochromators which select the desired X-ray wavelength and create the large vertical offset and compound refractive beryllium lenses (CRLs) to focus or to collimate the beam.
- (iii) Experimental hutch, containing the six-circle diffractometer, a liquid diffractometer and two optical tables with five degrees of freedom.
- (iv) Control hutch, containing the electronics, computers and a chemical fume hood.

(v) Laboratories: one general laboratory for P08 exists containing a UHV deposition chamber and a glove box. A microscopy hutch contains an AFM and an ellipsometer. A mechanical and an electrical laboratory is shared with beamline P09. A chemical laboratory and chemical cleanroom is available for all PETRA III users.

In the following, each of the parts will be explained in detail. The complete list of beam parameters is summarized in Table 3 in the optics section (§4.2).

4.1. Undulator and front-end

Undulators with a magnetic period of 29 mm serve as standard sources at many PETRA III scattering and diffraction beamlines (Barthelmeß *et al.*, 2008). At P08 this device is 2 m long (U29-2). The U29-2 undulator is fully tunable. This means that it delivers high flux in an energy range from 3.4 keV to 40 keV without any gap. The spectral brilliance and the flux integrated over the dominant harmonics are depicted in Fig. 1. As can be seen from the figure, the accessible energy range of P08 is slightly smaller than the energy range of U29-2 which is due to constraints of the optics. However, this limitation has no impact on the operation of P08. The undulator cell of P08 is permanently set to high- β . Typical values for the source size and divergence are listed in Table 2.

The front-end contains water-cooled high-power slits. They are used to shape the beam and to reduce the heat load on the optical elements in the optics hutch by cutting the low-energy halo around the beam’s central cone. Also available are graphite and CVD-diamond foils which can optionally be used to suppress unwanted low-energy photons. An overview of the PETRA III undulator front-ends has been published by Hahn *et al.* (2007).

The front-end components of beamline P08 are completely separated from the front-end of P09. This makes the operation of both beamlines fully independent. Also, the undulators of P08 and P09 can be moved without cross-correlation effects on the X-ray beam parameters.

4.2. Optics

A sketch of the optics of P08 is depicted in Fig. 2. The white X-ray beam is monochromated at the liquid-nitrogen-cooled

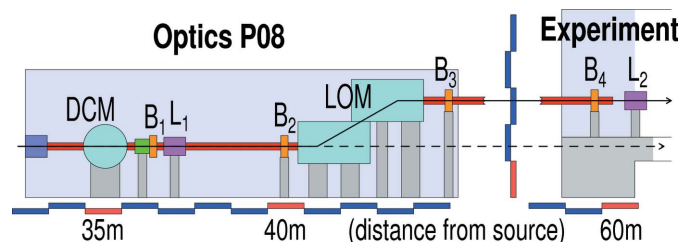


Figure 2
 Sketch of the P08 optics with double-crystal monochromator (DCM), beam position monitors (B_1 – B_4), CRL changers (L_1 and L_2) and large-offset monochromator (LOM). The dashed line is the beam path of beamline P09. The horizontal and vertical scales (blue and red displaced bars) show the dimensions.

double-crystal monochromator (DCM) (FMB Oxford, Osney Mead, UK) which is equipped with two Si 111 crystals reflecting the beam at a fixed offset of 22.5 mm with the option to tune this value by ± 1.5 mm if necessary. Beam position monitors (BPMs) (FMB-Oxford) right after the DCM enable X-ray beam stabilization by means of horizontal and vertical position and direction (accuracy better than 5 μm in position and better than 1 μrad in direction). Optionally, sets of compound refractive lenses (Lengeler *et al.*, 1999) can be used to collimate the X-ray beam (compensation of divergence) or to focus the beam (with a 1:1 imaging of the X-ray source to the sample position). If a focus of vertical size close to 2 μm is required, further lenses are available in the experimental hutch close to the sample position. A large-offset monochromator (LOM-1250) shifts the beam up by 1250 mm to separate P08 from P09. In the following the LOM-1250 and the focusing are explained in more detail.

4.2.1. Large-offset monochromator. The most striking device at the P08 optics is the double-crystal large-offset monochromator (Horbach *et al.*, 2010) which has been specially designed to (i) lift the beam up by the above-mentioned 1250 mm (as fixed offset), (ii) increase the resolving power of the X-ray beam and (iii) suppress the higher harmonic contamination of the X-ray beam.

From Fig. 2 it is obvious that the LOM-1250 lifts the beam up to sufficiently separate the P08 beam from P09. The resolving power in terms of energy bandwidth is determined by the reflecting pair of Si 311 or Si 511 crystals. With the natural divergence of the PETRA beam and Si 311, a typical bandwidth of $\Delta E/E \simeq 4 \times 10^{-5}$ can be obtained at photon energies between 5.4 and 18.4 keV. For energies between 8.4 and 29.4 keV the pair of Si 511 crystals delivers a bandwidth of $\Delta E/E \simeq 2 \times 10^{-5}$. This value can be decreased further on collimation (decreasing the opening angle of the beam) as angle and energy are linked *via* Bragg's law. The lower limit of the bandwidth is determined by the width of the Bragg reflection at parallel beams (Zachariasen, 1967). Using Si 511 this limit is at $\Delta E/E \simeq 1 \times 10^{-5}$ and can be approximately obtained at P08 when the lenses L_1 are used in collimation mode and the energy is around 9 keV. Thus, the energy resolution can be increased by a factor of ten compared with the beam from the Si 111 crystals of the DCM.¹

To compensate for slow drifts of the X-ray beam each of the LOM-1250 crystals is equipped with piezo actuators. Using the signals from the BPMs B_3 and B_4 the beam position can be stabilized in the micrometer range at the sample position which is not possible with the BPMs B_1 and B_2 alone (see Fig. 2).

A unique capability of the LOM-1250 is the higher harmonic suppression which is virtually perfect at P08. Generally, every beamline at a synchrotron radiation facility fights the contamination from high-energy photons. To reduce the flux of the high-energy photons, usually one or two X-ray mirrors with a combined suppression factor of typically 10^{-2} to 10^{-5} are used. At P08 the high harmonic suppression is

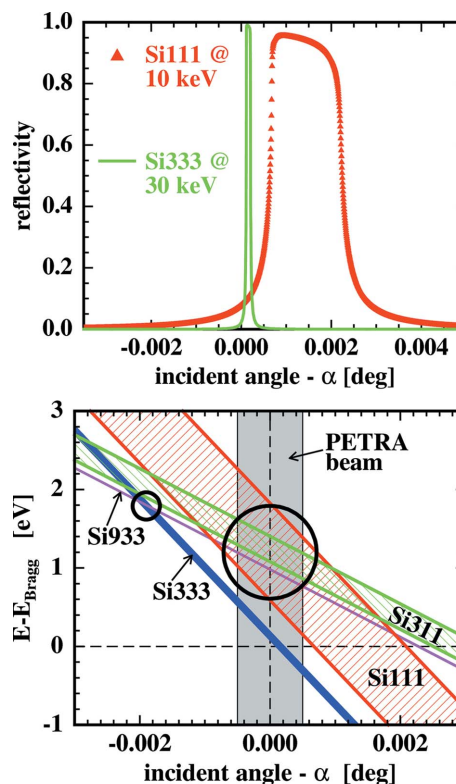


Figure 3

Top: calculation of symmetric Si 111 and Si 333 Bragg reflections at 10 keV and 30 keV, respectively. At these energies the Bragg angle α is 11.403° . Bottom: DuMond diagram of a Si 111–Si 311 pair reflecting at 10 keV. Besides the fundamentals the higher harmonics Si 333 and Si 933 at 30 keV are drawn. The outlined circles mark the intersection areas of the fundamentals and the higher harmonics whereas the gray area marks the PETRA beam divergence in the vertical.

obtained differently. We use the fact that the position of a Bragg peak in symmetric reflection geometry slightly differs from the Bragg angle depending on the photon energy and the index of the reflection (see the dynamical scattering theory; for example, Zachariasen, 1967). An example is shown in Fig. 3.

At P08 the DCM is equipped with a pair of Si 111 crystals whereas the LOM-1250 has pairs of Si 311 or Si 511 crystals installed. By tuning them to maximum flux throughput at the desired energy the higher harmonic reflections are automatically detuned and therefore strongly suppressed. This can be visualized by the so-called DuMond diagram (DuMond, 1937) which has been drawn in Fig. 3 according to the P08 set-up.

The DuMond diagram shows the reflecting areas of the Si 111 and Si 311 fundamental reflections and the Si 333 and Si 933 which correspond to the third harmonic. Both fundamentals intersect at the large outlined circle whereas the third harmonics intersect at the small one. Intersection in this context means that the X-rays can be reflected by both crystals. Fig. 3 also displays the vertical divergence of PETRA III. It is obvious that owing to the small divergence the fundamental and the harmonic cannot be reflected simultaneously. By correct tuning of the fundamental reflections to the center

¹ With a native bandwidth of 1×10^{-4} .

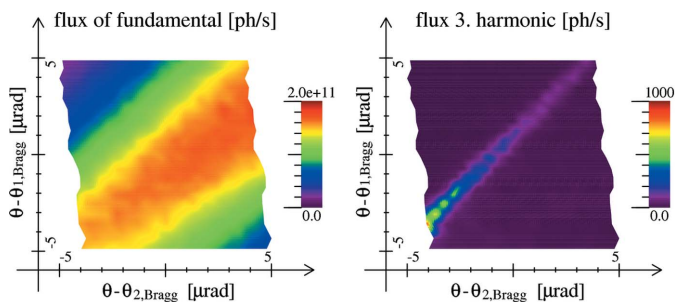


Figure 4 Flux of the fundamental (left) and the third harmonic (right) at 9 keV and 50 mA ring current using the Si 311 pair at the LOM-1250 of P08. The maximum of the fundamental reflection is outside the figure to the top right. The maximum of the third harmonics is at the far bottom left outside the figure. The x,y axes denote the detuning of the two LOM crystals.

of the PETRA beam the higher harmonics are suppressed by more than a factor of 10^8 at beamline P08. This number can be increased further by slightly detuning the second Si 111 crystals of the DCM which results in a virtually complete suppression of higher harmonics at a fundamental intensity of 10^{12} counts s^{-1} at 10 keV.

The suppression has been determined quantitatively. The flux of the fundamental and the third harmonic have been measured at a fixed photon energy of 9 keV using an energy-resolving detector and an attenuator which reduces just the flux of the fundamental. Data sets have been created depending on the tuning angle of the second crystal of the DCM and both tuning angles of the LOM-1250 crystals. The data show that the intersections of the fundamental and the third harmonic do not coincide at any of the data sets (see, for example, Fig. 4 for one particular position of the second DCM crystal). It turns out that the flux of the fundamental is about $3\text{--}4 \times 10^{11}$ counts s^{-1} (at 50 mA ring current) with less than 1000 counts s^{-1} in the third harmonics. At higher photon energies or when using the Si 511 crystals at the LOM-1250, no third-harmonic radiation can be detected at all. At lower energies than 8 keV (with wider reflections and larger divergence of the PETRA beam) the third-harmonic contamination is still less than 10^4 counts s^{-1} at 100 mA ring current.

4.2.2. Collimation and focusing. To shape the X-ray beam by means of divergence and beam size at the sample position a CRL changer (L_1 in Fig. 2) is used. It is positioned approximately in the center between the source and the sample at 63 m. The CRL changer consists of 12 packages of different sets of beryllium CRLs. Using adequate combinations of packages, focusing or collimation of the X-ray beam is possible for basically all photon ener-

gies of P08 above 7 keV. For some energies smaller than 7 keV the focal distance to the sample is not well matched owing to the limited number of available combinations.

For experiments with high resolution in reciprocal space (\mathbf{q} -space), beams with small divergence and small energy bandwidth are required as both determine the resolution $\Delta\mathbf{q}$ (Warren, 1990). In the so-called collimation mode (CM) the lenses L_1 collimate the beam in the vertical direction to $w'_v \simeq 2 \mu\text{rad}$ (FWHM) which is about one-fifth of the raw beam (raw mode, RM). In the horizontal direction the divergence w'_h is only 10 μrad as compared with 20 μrad for the uncollimated beam. The reason for the smaller effect in the horizontal is the larger horizontal source size. As the CRL changer is mounted between the DCM and the LOM-1250, the energy bandwidth becomes significantly smaller [see Fig. 3 (bottom) assuming a smaller width of the gray bar]. Depending on the selected crystal pair at the LOM-1250 (Si 311 or Si 511), using the CM the energy resolution is increased by a factor of three to four compared with the RM, which means an energy bandwidth $\Delta E/E \simeq 10^{-5}$.

Fig. 5 shows data of an experiment to determine the collimation. The rocking curves of three silicon Bragg reflections are shown: the 111, 222 and 333 reflections of a perfect single crystal of silicon. They have been measured in RM (top row) and in CM (bottom row) in vertical scattering geometry both using the Si 511 crystals in the LOM-1250.

The 222 reflection of silicon is not strictly forbidden as expected by crystal symmetry but exhibits a very small structure factor (Colella & Merline, 1966). Consequently, the Si 222 reflection has a very small width of approximately 0.2 μrad . This almost δ -function-like Bragg reflection is a very useful tool for measuring the resolution function.

The data have been analyzed using the exact energy- and angle-dependent resolution function of P08. For this it was assumed that the monochromator crystals are ideal and reflect

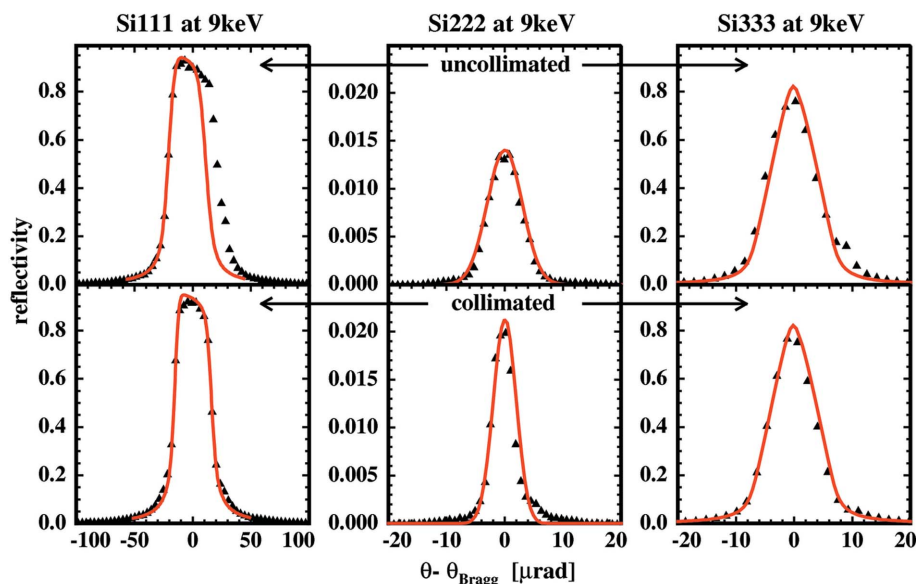


Figure 5 Measured (symbols) and calculated (lines) Bragg reflections of Si using the uncollimated RM (top row) and the CM (bottom row) at 9 keV and Si 511 crystals in the LOM-1250.

as given by the dynamical scattering theory for all reflections. The same applies for the silicon test sample. The calculation matches the data very well, concerning the shape and also the intensity which was not a free parameter. The resulting resolution function at 9 keV is a tilted rectangle in energy-angle space with the edges $\Delta E = (5 \pm 0.5) \times 10^{-2}$ eV, $w'_v = 6.5 \pm 0.2$ μrad and slope 0.02 ± 0.001 eV μrad^{-1} . The integrated flux is 2×10^{11} photons s^{-1} . These values show a gain by a factor of two in angular and energy resolution compared with RM.

The CRL changer L_1 can also be used in so-called focusing mode (FM). As the device is positioned approximately in the middle between source and sample the calculated focal spot has roughly the size of the source (FWHMs: $w_{s,h} \simeq 300$ μm in the horizontal and $w_{s,v} \simeq 12$ μm in the vertical, see Table 2). So far, the expected vertical value has only been obtained in a snapshot of 10 μs but not in a time average of 1 s. The reason for this is the liquid-nitrogen pump of the DCM; it creates vibrations of some hundred Hertz at the DCM crystals in the 100 nrad range which consequently limit the vertical spot size at the sample to 20 μm (in time average). Still, the FM is used very frequently: owing to the center position of the CRL changer the divergence of the X-rays remains unchanged as compared with the unfocused beam. This enables scattering experiments with small beam and very high q resolution.

If microfocusing is required, the second CRL changer L_2 in the experimental hutch can be used (so-called μ -mode or μM). With a distance of 1.5 m to the sample position of the six-circle diffractometer and 5.5 m to the liquid diffractometer a vertical beam size between 0.5 and 2 μm can be obtained theoretically, depending on the photon energy and prefocusing. A first measurement using the lenses L_2 at 25 keV and prefocusing with L_1 yielded a vertical beam size of 2 μm at the six-circle diffractometer (see Fig. 6).

4.2.3. Summary of the P08 beam parameters. Depending on the requirements of the users, different modes at different photon energies can be accommodated. At energies below 8.4 keV the Si 311 crystals at the LOM-1250 have to be used, above 18.8 keV the Si 511 crystals have to be taken. In the intermediate range the Si 311 pair can be used for high flux and the Si 511 pair for high-energy-resolution applications.

The CRLs L_1 and/or L_2 can be set for different applications. Without any lenses (raw mode) the highest flux at relatively large beam is obtained. Using some lenses of L_1 the beam can be collimated (collimation mode). In this mode the divergences and the energy resolution is smallest meaning the highest resolution power. With some more L_1 lenses moderate focusing is available (focusing mode) where at the sample position a vertical focus of 20 μm can be achieved at the same resolution as the raw mode. Finally, in

Table 3

List of the P08 X-ray beam parameters at the sample position.

The values correspond to the raw mode RM. The values for the other modes can be calculated by the rules given below. Units: flux, counts s^{-1} ; beam size (FWHM) $w_{h,v}$, μm ; divergence (FWHM) $w'_{h,v}$, μrad ; energy bandwidth, 10^{-4} .

Values in raw mode RM: LOM-1250 with Si 311					
	5.4 keV	8.4 keV	10 keV	14 keV	18.8 keV
Flux	2×10^{12}	2×10^{12}	1×10^{12}	2×10^{12}	1.5×10^{12}
w_h	1500	1400	1300	1300	1300
w_v	1000	850	850	800	800
w'_h	24	20	20	20	20
w'_v	16	14	13	13	11
$\Delta E/E$	0.3	0.3	0.4	0.5	0.6

Values in raw mode RM: LOM-1250 with Si 511					
	8.4 keV	14 keV	18.8 keV	24 keV	29.4 keV
Flux	8×10^{11}	7×10^{11}	5×10^{11}	4×10^{11}	2×10^{11}
w_h	1400	1300	1300	1300	1300
w_v	850	800	750	650	550
w'_h	20	20	20	20	20
w'_v	13	13	11	9	8
$\Delta E/E$	0.2	0.3	0.3	0.3	0.4

Values in collimation mode CM: flux $\times 0.7$, $w_{h,v} \times 0.5$, $w'_h \simeq 10$ μrad , $w'_v \simeq 2$ μrad , $\Delta E/E \times 0.4$

Values in focusing mode FM: flux $\times 0.5$, $w_h \simeq 300$ μm , $w_v \simeq 20$ μm , $w'_{h,v}$ as in table, $\Delta E/E$ as in table

Values in microfocusing mode μM : flux $\times 0.2$, $w_h \simeq 30$ μm , $w_v < 2$ μm , $w'_{h,v} \times 20$, $\Delta E/E$ as CM or RM

the μ -mode and using the lenses at L_2 (and L_1 if pre-focusing is required) a micrometer-sized focus in the vertical is possible. Table 3 summarizes the beam parameters at the different modes.

The accessible length scales in real space are determined by two properties: the upper limit is given by resolution, and the lower limit by the accessible q -range (given by the maximum scattering angle and the wavelength). The q -range is larger at higher photon energy whereas resolution is better at lower energies. Therefore, the accessible length scales at P08 strongly depend on the photon energy but also on the

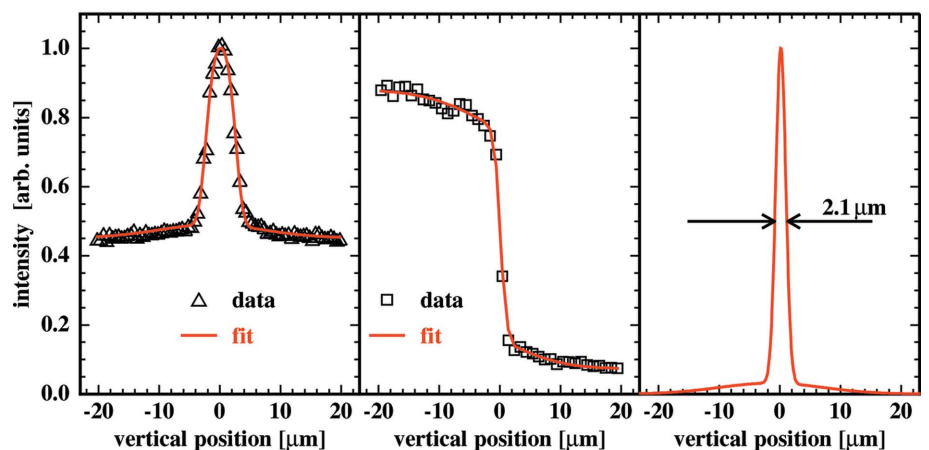


Figure 6 Determination of the spot size of a microfocus at 25 keV. Left: fluorescence signal from a 5.8 μm gold-coated tungsten wire. Center: knife-edge scan. Right: reconstructed vertical beam profile. The flux in the focus corresponds to 2×10^{10} counts s^{-1} .

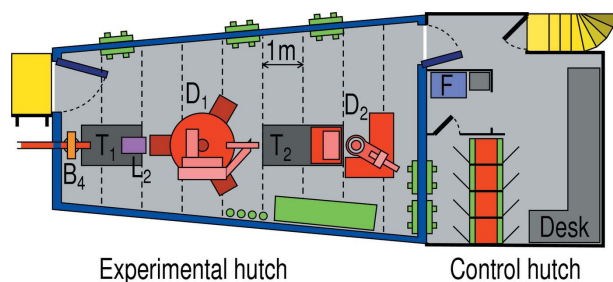


Figure 7
 Sketch of the experimental and control hutch of P08 with the X-ray beam coming from the left. The beam height over the floor is 1 m. Motorized optical tables are T_1 and T_2 . D_1 is the six-circle diffractometer and D_2 the liquid diffractometer. F denotes a fume hood in the control area. B_4 and L_2 are explained in Fig. 2.

experimental set-up such as slits and analyzers. Typical values at 8 keV are 80 μm with an accuracy of 5×10^{-5} for the lower limit and 5 μm for the upper limit. At 25 keV length scales between 30 μm with 10^{-4} accuracy and 1.5 μm are accessible.

4.3. Experimental and control hutch

The experimental hutch of P08 is roughly 9 m long and has an average width of 4.5 m and a height of 3.5 m. Temperature stability is better than 0.1 K if doors are closed. The beam height over the floor is 1 m. The control hutch contains, besides the work space, electro installations and a small fume hood for simple chemical preparation. Both hutches are sketched in Fig. 7.

On entering the experimental hutch the X-rays pass through the beam position monitor B_4 (see Figs. 2 and 7). Right after B_4 a 20 μm -thick diamond window of diameter 5 mm separates the optics vacuum from the experiment. Following that an optical table (T_1) (Instrument Design Technology, Widnes, UK) with a maximum load of 1 t is installed with a breadboard of length 1.5 m and width 1 m. Five encoder-controlled stepper motors enable pitch, yaw and roll movements of $\pm 1^\circ$ and two translations (vertical and horizontal, perpendicular to the X-ray beam) with ± 20 mm travel. The accuracy of the tilts is 1 μrad and of the travels 1 μm . The table T_1 is used to align the lens changer L_2 (see Fig. 2) for the μm . It also carries two pairs of motorized slits (JJ X-Ray A/S Kgs, Lyngby, Denmark), an X-ray flux monitor, a tunable attenuator (5–30 keV) and an X-ray eye.

The device D_1 is a high-precision (6 + 2)-circle diffractometer (Kohzu Precision, Kawasaki, Japan) with Eulerian cradle and analyzer stage. This diffractometer is specially designed to accommodate the small beam height of 1 m and is of extreme high precision (with 2×10^{-5} deg resolution of the main axes and less than 15 μm sphere of confusion; see Fig. 8).

The six-circle diffractometer is highly flexible since the sample can be mounted on two different φ, x, y, z stages. Standard is a high-precision stage with optional double goniometer which can be loaded with 10 kg load. Two sample cells are available: a HV oven with Be dome which has a temperature range from room temperature up to 723 K, and a vacuum oven with graphite dome (Model DHS1100, Anton Paar GmbH, Graz, Austria) with a temperature range from

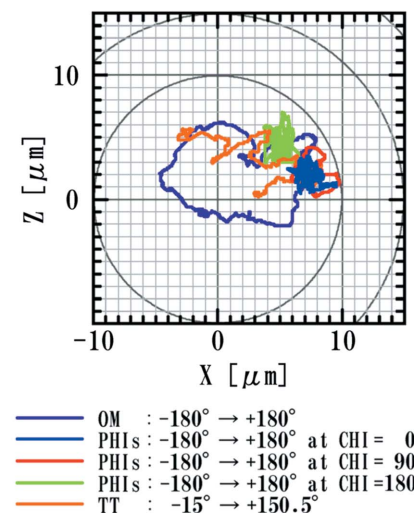
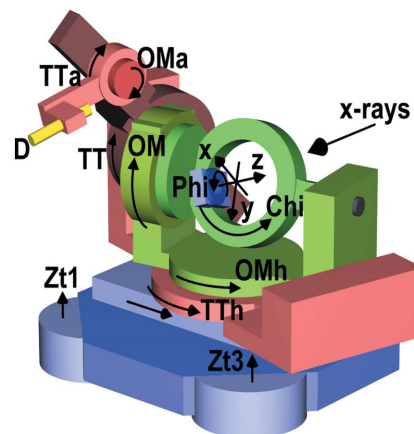
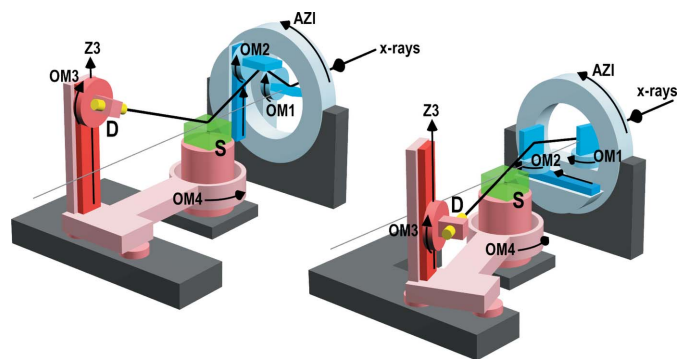


Figure 8
 Top: sketch of the six-circle diffractometer with the motor names according to the notation at P08 and a detector (D). Not shown is an optional double-tilt goniometer which can be mounted onto the xyz stage and an optional heavy-load χxyz stage. Bottom: the combined sphere of confusion of the main axes is smaller than 15 μm .

room temperature up to 1373 K. Other equipment can be accommodated on demand. Different detectors are available which fit the detector arm: a NaI scintillation counter and an avalanche photodiode (FMB-Oxford) as point detector, a $1280 \times 50 \mu\text{m}$ pixel line detector (Model Mythen 1k, Dectris, Baden, Switzerland), an energy-dispersive detector (Model Vortex EM, SII NanoTechnology USA, Northridge, CA, USA) and a 4096×4096 CCD with 15 μm pixel size (Princeton Instruments, Trenton, NJ, USA). Other detectors such as a 2048×2048 flat-panel with 200 μm pixel size (Model XRD 1621, PerkinElmer, Waltham, MA, USA) are also available. As an example of measurements taken at the six-circle diffractometer a crystal truncation rod measurement of an epitactic 001 bismuth layer grown on Si 111 crystal is shown in Fig. 10. An investigation of periodic dislocation networks which form in thin films of PbSe has already been published (Wintersberger *et al.*, 2010).

The diffractometer, the front-end, the optics components and the hardware on table T_1 are interfaced *via* the TANGO


Figure 9

Schematic sketch of the liquid diffractometer LISA at maximum (left) and zero incident angle (right). In black are the three independent supports which carry (in the beam direction) the beam filter, the sample tower (S) and the detector stage (D).

control system (Götze *et al.*, 2003). The user interface is a command line version of *SPECTRA/ONLINE* (Kracht, 2007).

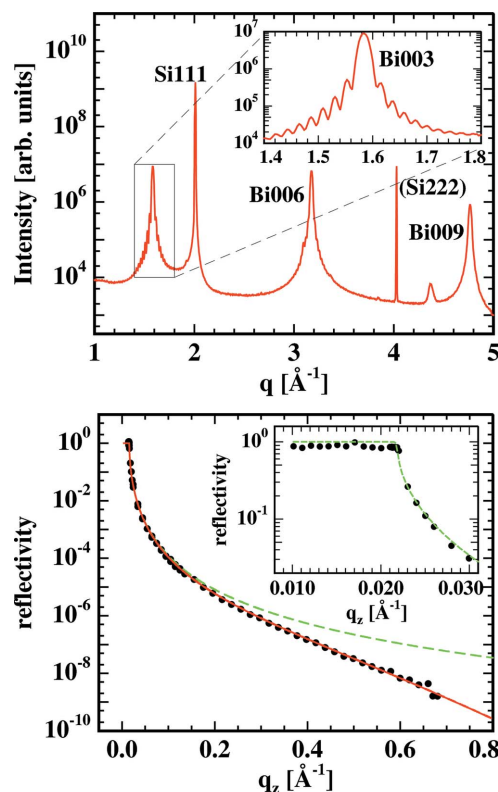
After the six-circle diffractometer, table T_2 and the diffractometer D_2 follow (see Fig. 7) where D_2 is the Liquid Interfaces Scattering Apparatus (LISA) designed at the University of Kiel, Germany (Murphy *et al.*, 2010, 2012). LISA is a dedicated diffractometer for surface or interface studies of samples such as liquids that cannot be tilted in order to achieve a non-zero incident angle. The three main modules of LISA are: the double-crystal beam filter on table T_2 , the sample tower and the detector tower D (see Fig. 9).

The beam filter is designed as a large azimuth rotation with its axis along the X-ray beam. It accommodates two silicon crystals which reflect at different angles, the first at the Si 111 Bragg angle and the second at the Si 220 Bragg angle (see Fig. 9). As a result the X-ray beam is tilted relative to the original incident beam, and the tilt angle defines the incident angle on the sample surface. By rotation around the AZI axis, different angles relative to the horizontal sample surface S can be obtained. The detector D is oriented adequately to detect the reflected beam from the sample.

On the left-hand side of Fig. 9, LISA is adjusted for the maximum incident angle on the sample surface, which in the present set-up corresponds to a wavevector transfer of $q_{\max} \simeq 2.6 \text{ \AA}^{-1}$ (roughly independent of the photon energy). On the right-hand side of this figure the incident angle is zero.

The great advantage of the LISA set-up is that the incident angle on the sample can be changed without moving the sample. For this, the three components of LISA are supported by completely independent structures. Table T_2 carries the beam filter, a small granite block is the base of the sample stage S, and the detector stage D is mounted on another separate granite block. Thus, at LISA the incident and exit angle can be moved without mechanically exciting the sample surface. An example measurement of water reflectivity taken at LISA is shown in Fig. 10.

The LISA diffractometer is controlled by *SPEC* (Swislow, 2009). Other critical beamline components can be accessed via a direct interface to *TANGO*. The hardware of LISA is compatible with DESY standards so that interfacing with


Figure 10

Top: crystal truncation rod scan of a crystalline bismuth film epitaxially grown on Si 111 taken at 18 keV. The oscillations show the film thickness. Bottom: reflectivity of a free water surface at 296 K obtained using LISA at 25 keV. The data (symbols) were recorded in ~ 1 h. The dashed lines show a zero-roughness calculation. The solid line includes the surface roughness which is induced by capillary waves.

TANGO is possible. A more detailed description of LISA has been published elsewhere (Murphy *et al.*, 2010).

4.4. Laboratories

For sample preparation and analysis the following laboratories are available: (i) a preparation laboratory with molecular beam epitaxy (MBE) chamber and glove box, (ii) an analysis laboratory with an atomic force microscope (Model SOLVER NEXT, NT-MDT, Zelenograd, Russia) and ellipsometer, both under responsibility of P08, (iii) a mechanical laboratory and (iv) an electrical laboratory including an optical microscope and fume hood. Laboratories (iii) and (iv) are both under shared responsibility of P08 and P09. Shared chemical laboratories with cleanroom facilities are available on request.

A UHV chamber system with base pressure 2×10^{-10} mbar is installed in the preparation laboratory of P08 to deposit thin insulator, semiconductor and metal films on top of insulator, semiconductor or metal substrates by means of MBE (see Fig. 11). The chamber A contains four storage places of which two can be heated to clean the substrates by e-beam or DC heating. Six MBE evaporators can be mounted on DN63CF UHV ports located at the bottom of chamber B. The deposition can be monitored by a RHEED (reflection high-energy electron diffraction) system. The sample on the five-axis

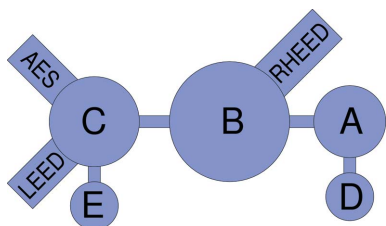


Figure 11

Sketch of the UHV chamber system in the P08 preparation laboratory with the following chambers: Storage and degassing (A), preparation (B) and analysis chamber (C), load lock (D) and baby chamber system (E).

manipulator can be heated by DC or e-beam and can be cooled by liquid nitrogen. After preparation the structure and chemistry of the samples can be investigated in chamber C by low-energy electron diffraction (LEED) and Auger electron spectroscopy (AES). For the future an additional atomic force microscope is planned to be installed in a further chamber located next to the analysis chamber. After this pre-characterization the sample can be transferred into the diffractometer *via* the baby chamber system equipped with an ion-getter pump. The sample growth and characterization is open to experienced UHV users in the framework of a cooperation with the P08 beamline staff.

5. Conclusion and outlook

At the third-generation synchrotron radiation source PETRA III the undulator beamline P08 has been accepting regular users since summer 2010. The X-ray beam is of extreme low divergence and energy bandwidth, even at moderate focusing. The infrastructure of P08 including the source, the optics and the diffractometers support high q -resolution X-ray scattering and diffraction studies of bulk and interface structures at solids and liquids. Sample preparation and characterization laboratories are available. In the future, the SAXS/GISAXS capabilities in combination with diffraction will be enhanced. Also, timing experiments will be accommodated by including a bunch clock at the beamline.

The authors would like to acknowledge U. Hahn, Th. Kracht and the FS-EC group, M. Hesse and the FS-BT

vacuum technology group, J. Spengler and the FS-TI group for the general infrastructure, and M. Tischer and the FS-US undulator group. Because of their work and efforts the beamline was operational in 2009 as one of the first beamlines of PETRA III. Also, we would like to thank D. Samberg and R. Döring for engineering and technical support at P08.

References

- Balewski, K., Brefeld, W., Decking, W., Franz, H., Röhlberger, R. & Weckert, E. (2004). *PETRA III Technical Design Report*. Deutsches Elektronen-Synchrotron DESY, Hamburg, Germany.
- Barthelmeß, M., English, U., Pflüger, J., Schöps, A., Skupin, J. & Tischer, M. (2008). *Proceedings of EPAC08*, p. 2320.
- Brefeld, W. (2010). *PETRA III Machine Parameters*, http://hasylab.desy.de/facilities/petra_iii/machine/parameters/index_eng.html.
- Colella, R. & Merline, A. (1966). *Phys. Status Solidi*, **18**, 157–166.
- DuMond, J. W. M. (1937). *Phys. Rev.* **52**, 872–883.
- Götz, A., Tarell, E., Pons, J. L., Meyer, M., Poncet, F., Heunen, G. & Götz, E. (2003). *Proceedings of ICALEPCS2003*, p. 220.
- Hahn, U., Peters, H. B., Röhlberger, R. & Schulte-Schrepping, H. (2007). *AIP Conf. Proc.* **879**, 539–542.
- Horbach, J., Degenhardt, M., Hahn, U., Heuer, J., Peters, H. B., Schulte-Schrepping, H., Donat, A. & Luedecke, H. (2010). In *16th Pan-American Synchrotron Radiation Instrumentation Conference (SRI 2010)*. Amsterdam: Elsevier.
- Kracht, T. (2007). *ONLINE*, <http://hasyweb.desy.de/services/computing/online/online.html>.
- Lengeler, B., Schroer, C., Tümmler, J., Benner, B., Richwin, M., Snigirev, A., Snigireva, I. & Drakopoulos, M. (1999). *J. Synchrotron Rad.* **6**, 1153–1167.
- Murphy, B. M., Greve, M., Runge, B., Koops, C. T., Elsen, A., Stettner, J., Seeck, O. H. & Magnussen, O. M. (2010). *AIP Conf. Proc.* **1234**, 155–158.
- Murphy, B. M., Greve, M., Runge, B., Koops, C. T., Elsen, A., Stettner, J., Seeck, O. H. & Magnussen, O. M. (2012). In preparation.
- Swislow, G. (2009). *Certified Scientific Software*. Cambridge, MA, USA.
- Tanaka, T. & Kitamura, H. (2001). *J. Synchrotron Rad.* **8**, 1221–1228.
- Thompson, A. C. & Vaugan, D. (2001). *X-ray Data Booklet*. Lawrence Berkeley National Laboratory, Berkeley, CA, USA.
- Warren, B. E. (1990). *X-ray Diffraction*. New York: Dover.
- Wiedemann, H. (2003). *Synchrotron Radiation*. Berlin: Springer.
- Wintersberger, E., Hrauda, N., Kriegner, D., Keplinger, M., Springholz, G., Stangl, J., Bauer, G., Oswald, J., Belytschko, T., Deiter, C., Bertram, F. & Seeck, O. H. (2010). *Appl. Phys. Lett.* **96**, 131905.
- Zachariasen, W. H. (1967). *Theory of X-ray Diffraction in Crystals*. New York: Dover.